Photoelectrodes Based upon Mo: $BiVO_4$ Inverse Opals for Photoelectrochemical Water Splitting

Min Zhou,[†,‡] Jian Bao,[†] Yang Xu,[‡] Jiajia Zhang,[†] Junfeng Xie,[†] Meili Guan,[†] Chengliang Wang,[‡] Liaoyong Wen,[‡] Yong Lei,[*,‡] and Yi Xie[*,†]

[†]Hefei National Laboratory for Physical Sciences at the Microscale, Department of Chemistry, University of Science & Technology of China, Hefei, Anhui 230026, China and [‡]Institute for Physics and IMN MacroNano® (ZIK), Technische Universität Ilmenau, Ilmenau, 98693 Germany

ABSTRACT $BiVO_4$ has been regarded as a promising material for photoelectrochemical water splitting, but it suffers from a major challenge on charge collection and utilization. In order to meet this challenge, we design a nanoengineered three-dimensional (3D) ordered macro-mesoporous architecture (a kind of inverse opal) of Mo:$BiVO_4$ through a controllable colloidal crystal template method with the help of a sandwich solution infiltration method and adjustable post-heating time. Within expectation, a superior photocurrent density is achieved in return for this design. This enhancement originates primarily from effective charge collection and utilization according to the analysis of electrochemical impedance spectroscopy and so on. All the results highlight the great significance of the 3D ordered macro-mesoporous architecture as a promising photoelectrode model for the application in solar conversion. The cooperating amplification effects of nanoengineering from composition regulation and morphology innovation are helpful for creating more purpose-designed photoelectrodes with highly efficient performance.

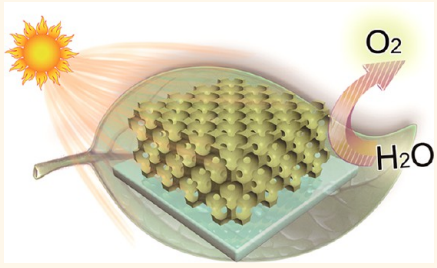

KEYWORDS: solar water splitting · bismuth vanadate · composition regulation · morphology innovation · template

Drawing inspiration from nature, photoelectrochemical (PEC) water splitting based on Fujishima–Honda effect[1] has been demonstrated as a feasible and cost-effective realization of an artificial analogy to photosynthesis.[2−7] With the goal of solar energy harvesting and storage, semiconductor photoelectrodes hold great promise to be an attractive alternative to the naturally occurring photosystems. In spite of intense research efforts, progress in this domain seems relatively slow because it is hard to find an ideal material that originates from the competing nature of its intrinsic properties.[8] Among all the widely investigated photocatalysts, monoclinic scheelite $BiVO_4$ is a promising candidate after striking a balance among various intrinsic features due to its suitable band gap, proper band location, great stability, and environment friendliness.[9,10] Despite these attractive characteristics, $BiVO_4$ still suffers from several challenging technical points for large-scale implementations. The primary one is a relatively low mobility of photogenerated charges, which would naturally hinder the separation of electron–hole pairs and consume some solar conversion efficiency. Accordingly, even from the viewpoint of a perfect bulk single-crystalline $BiVO_4$, both calculated and experimental[11−13] results indicate that alleviating charge migration problems, including surface charge transfer and bulk charge transport, shows a significant scope for improving the performance of PEC water splitting.

In general, charge migration is strongly affected by the crystal structural features and the morphology of a photoelectrode.[14,15] To meet the challenge of low charge migration in $BiVO_4$ photoelectrodes, first, we can regulate the composition by doping to increase the electronic conductivity intrinsically. For example, incorporation of Mo^{6+} into the partial sites of V^{5+} in $BiVO_4$ can change the crystal symmetry of $BiVO_4$ and introduce some polarons, both of which would benefit for higher charge carrier concentration.[16−20] Second, another efficient way to improve charge migration is to reduce the charge recombination during drift, diffusion, and surface transfer processes.[21]

* Address correspondence to yong.lei@tu-ilmenau.de, yxie@ustc.edu.cn.

Received for review April 10, 2014 and accepted June 9, 2014.

Published online June 09, 2014
10.1021/nn501996a

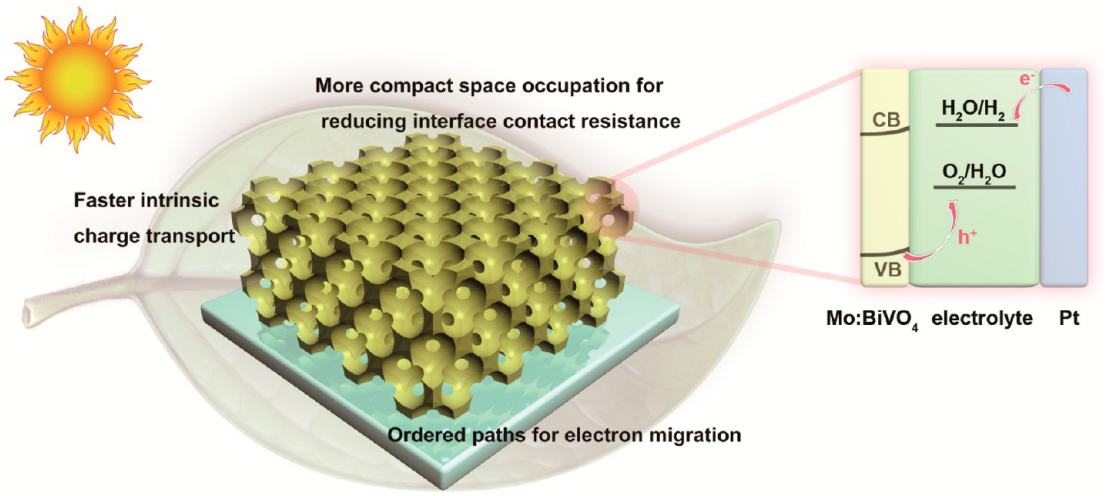

Scheme 1. Ideal schematic representation of the expected advantages of integrative Mo:$BiVO_4$ macro-mesoporous photoelectrodes.

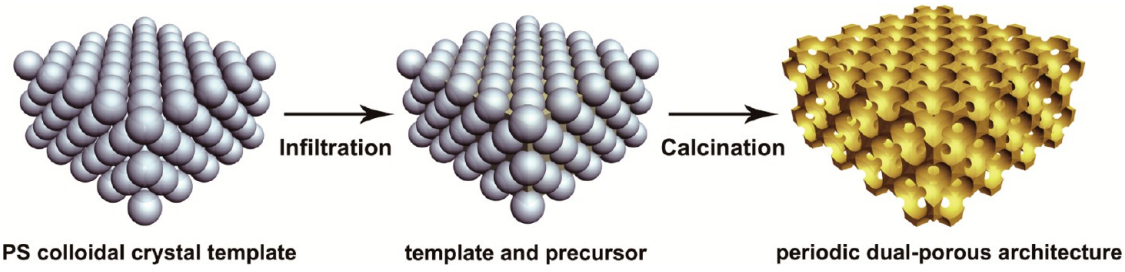

Scheme 2. Schematic illustration of the fabrication of Mo:$BiVO_4$ three-dimensional ordered macro-mesoporous architecture.

However, conventional $BiVO_4$ photoelectrodes are prepared through metal−organic decomposition or electrodeposition processes.[22−24] The disordered geometrical structures would increase the distance that charges must travel, and then charges would suffer from more nonproductive consumption due to increased chances of recombination. Fortunately, nanofabrication offers an opportunity for morphology innovation, enabling high surface reactive junction area and near-unity collection efficiencies. A three-dimensional (3D) ordered macro-mesoporous architecture (a kind of inverse opal) can serve as an efficient candidate for aforementioned requirements of improved charge migration.[25−27] By coincidence, interconnected periodic macroporous architectures can provide long-range-ordered paths for electron transport throughout the electrode.[27] Incorporating additional mesoscale pores can further increase the area of electrode/electrolyte junction and electrode/current collector junction. Utilization of holes and transport of electrons can be therefore accelerated. Overall, as shown in Scheme 1, an engineered 3D ordered macro-mesoporous Mo:$BiVO_4$ architecture is expected as a propitious model to meet the challenging point of low charge migration and further optimize the PEC performances of $BiVO_4$.

Inspired by this concept, we realize an innovative design of nanoengineered 3D macro-mesoporous Mo:$BiVO_4$ architecture through a controllable colloidal crystal template method. As a return for this design, superior photocurrent densities are achieved within expectation. This enhancement originates primarily from effective charge migration according to the analysis of PEC performance and electrochemical impedance spectroscopy. In this regard, the synergistic effects of nanoengineering from composition regulation and morphology innovation show great significance of designing highly efficient photoelectrodes for the application in solar conversion. Morphology innovation is more advantageous for the photoelectrodes with faster charge transport.

RESULTS AND DISCUSSION

The realization of this tentative idea needs feasible and straightforward procedures. Being a technologically facile approach, colloidal crystal template method is chosen here for fabricating the 3D ordered macro-mesoporous scaffold. Scheme 2 outlines the typical procedures of the general solution approach. First, a large-scaled colloidal crystal template is assembled using polystyrene spheres (PSs). Second, interstices in colloidal crystal template are infiltrated with precursor solution that solidifies *in situ* to form an intermediate composite structure. Finally, the template is removed through calcination. A 3D ordered macroporous host scaffold can be obtained topologically from the

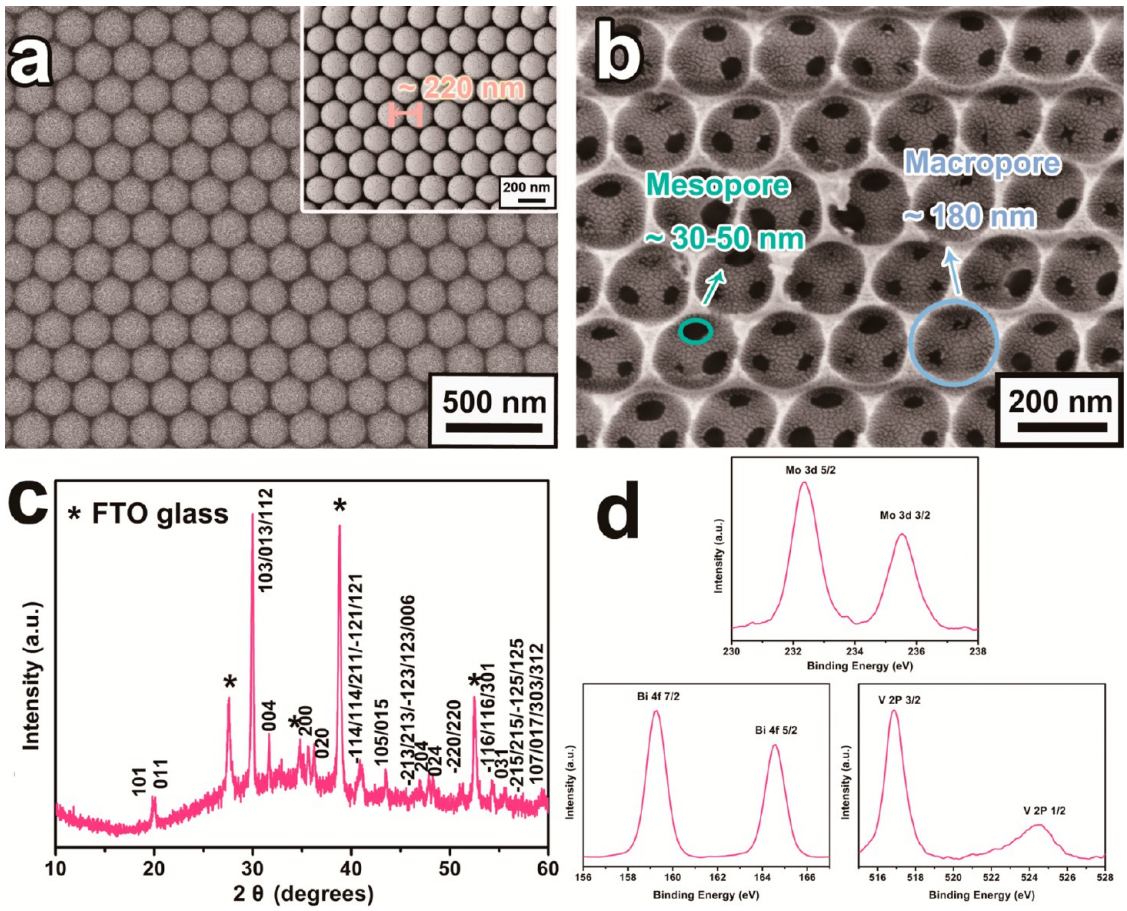

Figure 1. (a) Typical SEM image of colloidal crystal template of 200 nm PSs. Characterizations of three-dimensional ordered macro-mesoporous Mo:$BiVO_4$ architecture: (b) SEM image, (c) XRD pattern, (d) XPS data.

template with a high degree of periodicity in three dimensions. Compared with single-metal oxide, the principal difficulty for quaternary material is the choice of precursors for infiltration. Some common infiltration (*e.g.*, atomic layer deposition, electrodeposition) possesses many limitations of complex precursors and instruments. Solution infiltration approach offers the possibility for promoting compositional controllability, especially for quaternary materials. On the premise that the wettability and homogeneity can be guaranteed, the precursor solution would be arbitrarily chosen. From the viewpoint of developing an economical route for quaternary material architectures, herein a precursor solution consisting of low-cost metal salts is utilized instead of metal alkoxide.

To verify aforementioned tentative steps, Figure 1b shows the typical SEM image of the Mo:$BiVO_4$ 3D ordered porous architecture, which is the replica translated from the periodic colloidal crystal template using PSs with ~200 nm diameter (Figure 1a). When carefully observing the SEM image, we find that geometrical characteristics are mainly determined by two kinds of pores: one is the macropores surrounded by the skeletal walls with a diameter of ~180 nm; the other is the pores between neighboring macropores with a diameter of 30−50 nm. Commonly, porous materials are classified into several types by their diameters. According to International Union of Pure and Applied Chemistry (IUPAC) notation,[28] a mesoporous material contains pores with diameters between 2 and 50 nm, and a macroporous material is the material that possesses pores with diameters greater than 50 nm. In this sense, we realize the rational design of nanoengineered 3D ordered macro-mesoporous architecture. The XRD and XPS characterizations confirm the pure phase of $BiVO_4$ after doping.[7] From XPS results, two characteristic peaks located at 232.5 and 235.5 eV arising from $3d_{5/2}$ and $3d_{3/2}$ signals are assigned to the +6 oxidation state, suggesting that Mo cations are mainly present as Mo^{6+} into the lattice of the V places in $BiVO_4$.[16−18]

During all the steps, the colloidal crystal template is always heated for several minutes before infiltration at a temperature that is a little higher than its glass transition temperature (T_g) so as to increase the structural stability and to prevent structural dispersion.[29−32] This process will also lead to the deformation of neighboring PSs with different extent. Endowed with these interconnected parts, another kind of pore can be introduced into the macroporous host scaffold like a

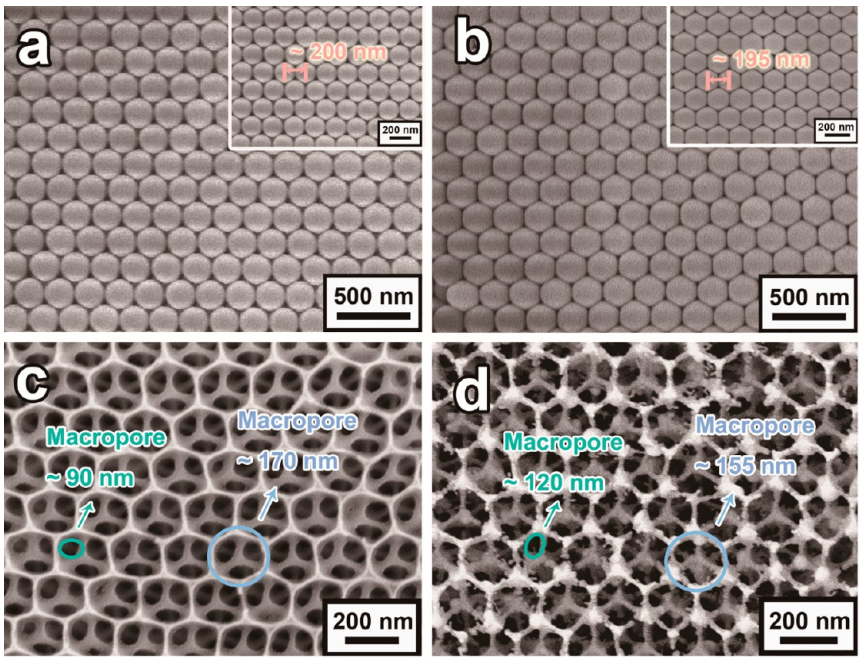

Figure 2. Typical SEM images of (a,b) deformation of the PS template for different time of post-heating treatment and (c,d) corresponding Mo:$BiVO_4$ three-dimensional ordered macro-macroporous architectures.

window between each macropore because of topological transition. The diameter of windows can be tuned easily from macroscale to mesoscale by carefully controlling the contact area between each sphere where the precursor solution cannot reach as long as the complete topological transition can be granted. Since the common precursor solution is not viscid enough to realize a high filling fraction, a key factor enabling our design is the usage of a sandwich infiltration method according to our previous work,[26] as shown in the Experimental Section. It is not necessary to heat the template, and thus the diameter of windows decreased. If the time of post-heating treatment is increased from 0 to 3 min and finally to 10 min (as illustrated in Figures 1a and 2a,b), the deformation caused by heating leads to gradual contact evolution between neighboring PSs from nearly no contact to quasi-point contact to quasi-facet contact, associated with the slightly reduced distance between neighboring spheres from 220 to 200 and 195 nm. The interstices among the PSs become smaller and smaller correspondingly. So after calcination, mesoscale pores (Figure 1b) gradually enlarge to macropores (~90 nm) and larger macropores (~120 nm) as shown in Figure 2c,d.

To quantify the solar water splitting activity of the 3D macro-mesoporous Mo:$BiVO_4$ architectures, we employ PEC cells and measure photocurrent densities of the cells. In order to demonstrate our hypothesis of cooperative amplification from nanoengineering, we analyze the PEC performances on various samples: (i) macro-macroporous Mo:$BiVO_4$ that serves as the reference sample for incorporating the mesoscale pores; (ii) disordered porous Mo:$BiVO_4$ to show the effects of incorporating the macroporous skeleton and mesoscale windows; (iii) macro-mesoporous $BiVO_4$ using as a reference sample for composition regulation; (iv) disordered porous $BiVO_4$ to illustrate cooperative amplification from nanoengineering through composition regulation and morphology innovation. All five architectures are directly fabricated on FTO glasses with the similar calculated maximum photocurrent densities under 1 sun AM 1.5 sunlight.[14,26,33] Corresponding characterizations are exhibited in Supporting Information Figures S1−S5. The XRD patterns and XPS peaks indicate that all the Mo-doped and nondoped monoclinic phase $BiVO_4$ matrix have high crystallinity and purity. All of the measurements here are carried out following optimization of the concentration of doping ions (Mo^{6+}) for photocurrent density. Since higher or lower concentration will reduce the overall performances, the value is set to 2 atom % at the vanadium sites ($BiV_{0.98}Mo_{0.02}O_4$) according to previous literature[10,24] and our experiments on optimizing the photocurrent densities.

Successful implementation of our designed approach can produce a photoelectrode with excellent PEC performance. Figure 3a shows linear sweep photovoltammetry measurements to determine the photocurrent density of the five kinds of photoelectrodes. Analysis of the photocurrent densities on various samples allows us to draw the following three conclusions. (i) Upon introduction of molybdenum, photocurrent densities are enhanced significantly across the entire potential range. (ii) All of the three 3D ordered macroporous-based photoelectrodes achieve

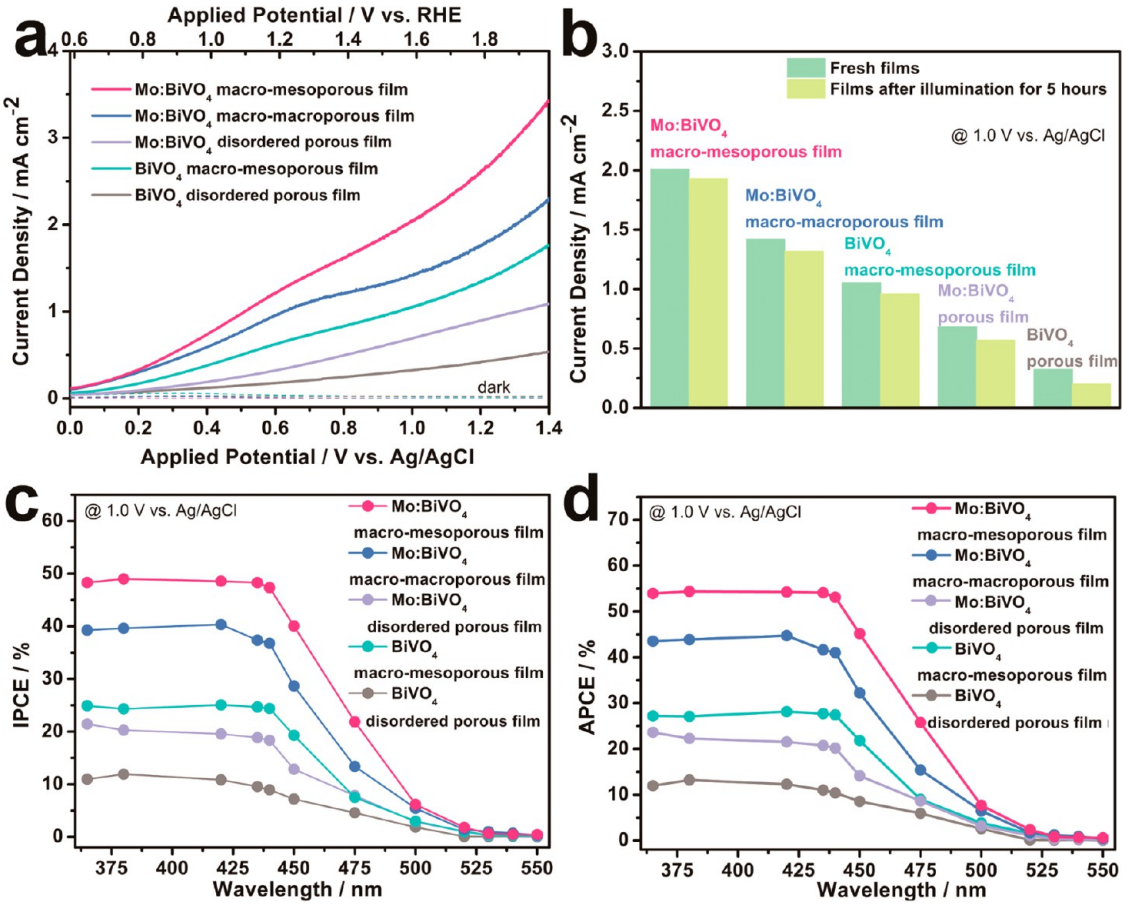

Figure 3. (a) Photocurrent density−potential curves (solid line) and dark-current density−potential curves (dashed line) of various films (scan rate = 10 mV s^{-1}). (b) Photocurrent density stability of various films at 1.0 V *vs* Ag/AgCl. The films for measurement are fresh and after illumination for 5 h, respectively. (c,d) IPCEs and APCEs of various films as a function of the wavelength at 1.0 V *vs* Ag/AgCl.

photocurrent densities of a few mA cm^{-2} under light illumination, which implies that the 3D ordered macroporous architecture is an appropriate model as a photoelectrode for PEC water splitting. As shown in Figure 3b, the superior photocurrent densities can also be observed after illumination for 5 h, which originate from the high stability of 3D ordered macroporous skeletons for keeping such a high performance. (iii) Compared to macro-macroporous photoelectrodes, our macro-mesoporous photoelectrodes show obviously enhanced photocurrent densities over the entire bias range. Typically, at the bias of 1.0 V *vs* Ag/AgCl, the photocurrent density of the macro-mesoporous photoelectrode is 2.0 mA cm^{-2}, which is 1.5-fold greater than the photocurrent densities of the macro-macroporous photoelectrode. It is expected that, since the macroscale sizes are identical to those photoelectrodes, the smaller mesoscale pores would provide a higher area of electrode/electrolyte junction and more contact area between electrode and current collector. The incident photon-to-electron efficiency (IPCE) mirrors the substantial enhancements of the photocurrent densities across the entire functional wavelength (Figure 3c). The IPCEs of the macro-mesoporous Mo:$BiVO_4$ photoelectrode reach a high value of ~40% at 1.0 V *vs* Ag/AgCl. Considering the similar calculated maximum photocurrent density of the five photoelectrodes (*i.e.*, similar absorbed photon flux), we assert that the differences of the photocurrent densities among the five samples can be fully ascribed to the differences in their photon utilization behaviors, which depends on the charge migration (including transfer and surface reactions). To elucidate the detailed effects of incorporating macroporous scaffold/mesoscale windows and doping for charge migration, the internal quantum efficiency, also so-called absorbed photon-to-electron conversion efficiency (APCE), is used to evaluate the capability of actual utilization of the photons more clearly in Figure 3d. These excellent APCE results confirm the synergistic improvement of nanoengineering from composition regulation and morphology innovation for charge migration in PEC water splitting.

In order to explore the details for the enhancement, at least two factors, composition regulation and morphology innovation, should be considered for charge migration carefully. As for composition regulation, depending on the types and degrees of doping (including the formation of solid solutions), changes

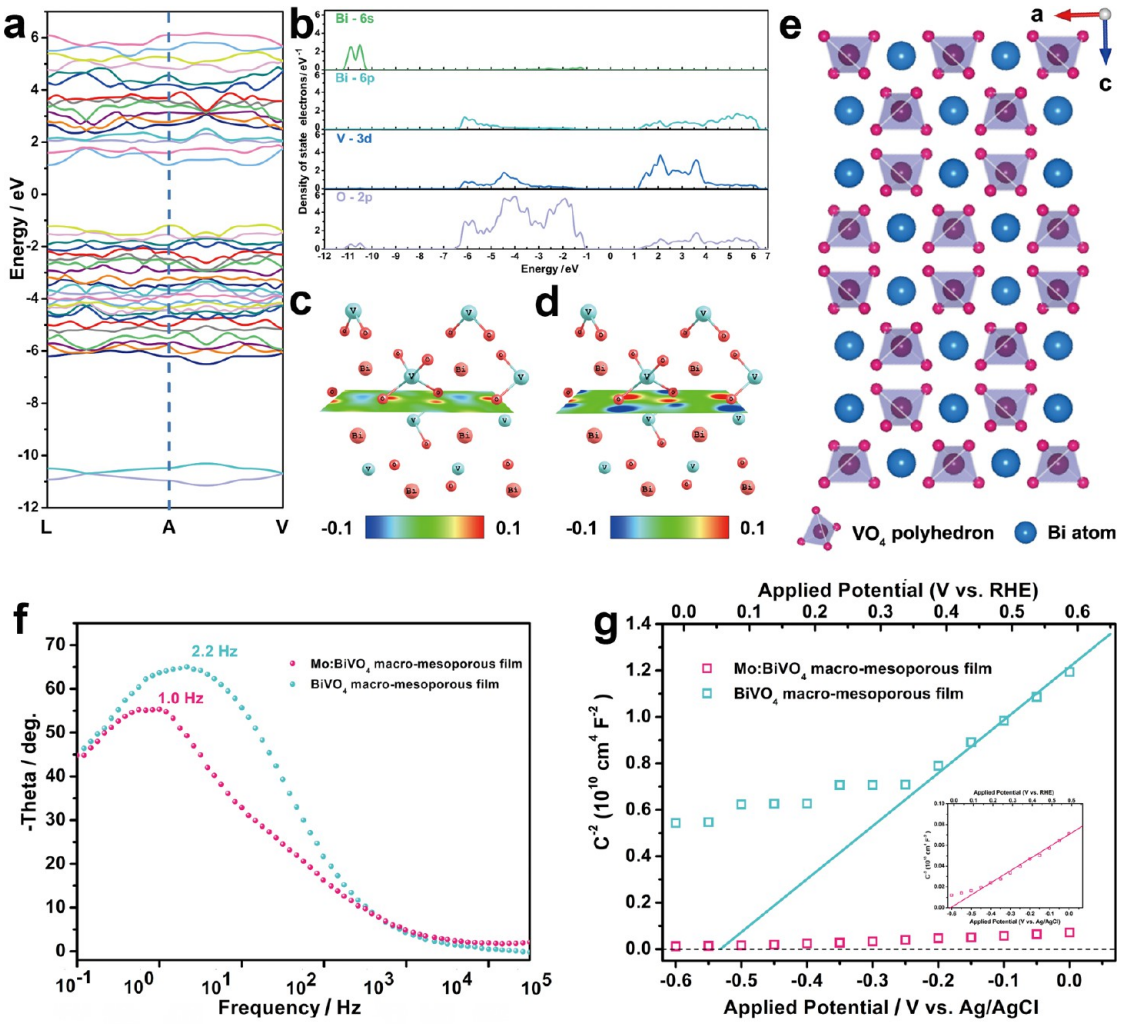

Figure 4. Calculated (a) electronic band structure, (b) electronic density of states; charge density contour plots projected along a (001) plane are shown for the two bands of (c) conduction band minimum and (d) valence band maximum at the A point (plotted from −0.1 (blue) to 0.1 (red) e·Å^{-3}). (e) Atomic supercell structures of monoclinic scheelite $BiVO_4$, from which the 2 × 1 × 2 tunneled structure and the interconnected VO_4 tetrahedra can be observed clearly. (f) Bode phase plots of electrochemical impedance spectra of macro-mesoporous $BiVO_4$ before and after introduction of molybdenum. (g) Mott−Schottky plots of macro-mesoporous $BiVO_4$ before and after introduction of molybdenum.

in charge migration can be expected. However, the effects of doping may not always be favorable because it will enhance electron−hole recombination, impede charge transport by providing scattering centers, and decrease the width of the depletion layer. Therefore, identifying appropriate dopants and their concentrations are important to increase the overall performances of the photoelectrodes. According to previous literature, various ions[10,11,16,17] have been introduced into partial sites of V^{5+} in $BiVO_4$. Among them, Mo^{6+} ion has been demonstrated as an n-type dopant to enhance $BiVO_4$ PEC performances, which can be evidenced by the positive slope from Mott−Schottky plots in Figure 4g.

As analyzed in density functional theory calculations (Figure 4a−d), we find that the fundamental reasons for low charge transfer are that the conduction band of $BiVO_4$ mainly consists of V 3d orbitals. Unfortunately, VO_4 tetrahedra in $BiVO_4$ are not connected with each other, as shown in Figure 4e.[34] So free electrons in $BiVO_4$ have to hop between VO_4 tetrahedra, leading to poor electron mobility. With the help of the substitutional defect of V^{5+} being replaced by Mo^{6+}, the shift of the (004) diffraction peak of $BiVO_4$ using FTO as the internal standard indicates the extension of *c*-axis after Mo doping (Figure S6a).[35−37] Besides, the crystalline symmetry also changes from monoclinic to approximate tetragonal structure like the changes in W:$BiVO_4$, evidenced by the (200) and (020) peaks which have been shifted toward one another (Figure S6b).[24] This crystal deformation caused by larger tetrahedral ionic radii of Mo^{6+} (tetrahedral ionic radii for V^{5+} and Mo^{6+} are 0.35 and 0.41 Å) may help to overcome poor electron mobility in pure $BiVO_4$ intrinsically.[11] Another aspect is that Mo^{6+} has one more valence electron than the V^{5+} host atom; hence their substitution into the host lattice can serve as electron donors.[17] Excess charge carriers may form small and/or large polarons

(*e.g.*, an electron with associated polarization field extending short or long distance) involving a sizable lattice distortion around the reduced V^{4+} ion; the former polarons localize at the atomic scale, and the latter polarons are extended over several lattice sites. For Mo-doped cases, the excess electron residing at the V^{4+} site may undergo migration to an adjacent V^{5+} (or Mo^{6+}) site, and a higher concentration of polarons would lead to a larger overlap between them, thereby lowering the activation energy for polaron hopping, resulting in enhanced charge carrier mobility and reduced resistance.

Outwardly, from the Bode phase plots for different $BiVO_4$ photoelectrodes at the open-circuit voltage (V_{OC}) of the PEC cells, the characteristic maximum frequency peaks (f_{max}) decrease obviously after doping. Generally speaking, there is no current passing through the external circuit at V_{OC}; meanwhile, all the electrons injected into the conduction band must be the reacted electrode/electrolyte interface. Thus, the lifetime of electrons for recombination with a time constant (τ_n) is correlated with f_{max} as this equation:[38]

$$\tau_n = 1/(2\pi f_{max})$$

As presented in Figure 4f, the maximum frequency value decreases with incorporating mesoscale pores and doping from ~2.2 to ~1 Hz, indicating that Mo:$BiVO_4$ possesses a 2-fold improved lifetime of electrons than that of undoped $BiVO_4$. Therefore, a low recombination rate is highly desired to achieve high charge collection efficiency, eventually leading to high solar conversion efficiency. Additional evidence comes from the slope of the linear part in the Mott−Schottky curves in Figure 4g; we can obtain carrier density to better validate the aforementioned two merits about charge migration upon the introduction of Mo^{6+}. Since the incorporation of dopants does not affect the morphology or the surface area of the electrode significantly, as shown in Figures 1c and S4a, the slope can be used to compare the relative carrier densities before and after doping. Here, macro-mesoporous Mo:$BiVO_4$ photoelectrode shows a lower slope and higher carrier density of 0.93×10^{21} cm^{-3}, whereas this value is only 2.64×10^{19} cm^{-3} for macro-mesoporous $BiVO_4$. In general, the increase in charge carrier density is associated with increased electrical conductivity (σ) of the photoelectrode as shown below:

$$\sigma = en\mu$$

where e is the electronic charge, n is the concentration of charge carriers, and μ is the mobility of the charge carriers. Increased mobility is highly favorable for improving charge transport and charge separation processes during PEC water splitting. Moreover, higher carrier density will raise the Fermi level of Mo:$BiVO_4$ toward its conduction band, which can create more significant band bending in the space charge region than that of bare $BiVO_4$ due to a larger difference between the Fermi level of Mo:$BiVO_4$ and the redox potential of the electrolyte. The enhanced electric field in the space charge layer facilitates the charge separation and slows the charge recombination rate. Although the doping mechanisms cannot be simply concluded from this analysis, it is speculated that the significant enhancement in photocurrent density is credited to its increased charge migration because of higher electrical conductivity and charge separation. We are interested to see if the addition of Mo is particularly useful to solve the key issues of poor conductivity.

With the above understanding of composition regulation, we next seek to observe how the 3D macro-mesoporous nanostructures behave upon enhanced charge migration during PEC water splitting. For this objective, we assess the dynamics of water oxidation at the $BiVO_4$/electrolyte interface and charge recombination by virtue of photocurrent transient decay. To summarize, three samples with different morphology (macro-mesoporous, macro-macroporous, and disordered porous Mo:$BiVO_4$ films) are held at a bias of 1.0 V *vs* Ag/AgCl, while illumination is turned on and off. The inset of Figure 5a shows an idealized photocurrent transient profile of the photoelectrodes. When the electrode is illuminated, the transient photoinduced separation of photoinduced charge pairs shows up as relatively large photocurrent spike (I_{in}). The spike then decays as the charge carriers migrate from the interior to the surface (electrons to the FTO and holes to the electrolyte). A subsequent decrease in the photocurrent indicates that the recombination occurred within the photoelectrode. A steady-state photocurrent (I_{st}) is achieved once the charge generation and recombination rates reach equilibrium. With all else being fundamentally equal, low recombination rates would give rise to long transient decay times. To know more details, we examine the transient decay time τ *via* a logarithmic plot of the parameter D, given by the equation[39,40]

$$D = (I_t - I_{st})/(I_{in} - I_{st})$$

where I_t is the photocurrent at time t (s) and I_{st} is the steady-state photocurrent. The transient time constant (τ) is defined as the time at which $\ln D = -1$.[39,40] The method allows a qualitative comparison of the electron lifetime within these photoelectrodes. Figure 5a compares the logarithmic plots of the photocurrent density transient decay D and τ of these photoelectrodes at 1.0 V *vs* Ag/AgCl. Both 3D macroporous-based photoelectrodes possess longer τ than disordered photoelectrode (1.1 s), indicating that the 3D macroporous skeleton plays a positive role in suppressing charge recombination and improving charge migration. Looking over the curves of normalized plots of photocurrent−time dependence, we find that τ has an obvious

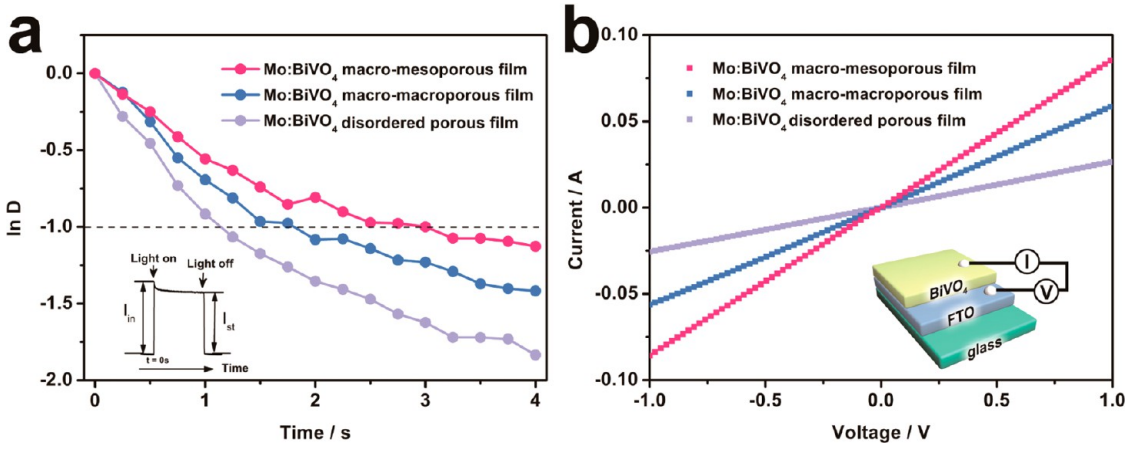

Figure 5. (a) Normalized plots of photocurrent density−time dependence of the nanowall-based films at 1.0 V *vs* Ag/AgCl. The inset represents a typical photocurrent transient response. (b) Typical current−voltage (*I*−*V*) characteristics with a schematic view of the device inset of the films.

improvement to 3.0 s after introducing mesoscale windows into the macropore skeleton. With a view to the few influences originating from similar carrier density and flat voltage, as shown in Figures 4g and S7, the trend between τ and morphology inspires us to further examine the resistance of three films to obtain more insight into charge transport within the films and the electrical contact with the current collector. As shown in Figure 5b, the resulting symmetrical and linear appearance indicates the Ohmic contacts between the film and the substrate.[37,40] The macro-mesoporous architecture possesses the smallest resistance for charge transfer, resulting in facile charge transport.

As seen from the photocurrent densities and the electrochemical impedance measurements, 3D ordered macro-mesoporous Mo:$BiVO_4$ provides multiple beneficial effects: First, interconnected 3D ordered macroporous architectures can provide long-range-ordered paths for electron transport throughout the electrode. In common, photoactivity of $BiVO_4$ is limited by its rapid charge recombination upon excitation, the suppression of which contributes to improving the overall photocurrent generation and catalytic reaction. Charge recombination is always promoted by the existence of many grain boundaries among particles as well as poor contact with the FTO surface. With respect to macro-mesoporous architectures, it can be imagined that the thick wall forms within the interstitial spaces, which is not as fragile as macro-macroporous architectures during the calcination process. Hence, a more compact packing of Mo:$BiVO_4$ grains contributes to easier charge transport and less recombination centers. Meanwhile, intact interfacial contact between materials and current collector minimizes the contact resistance at this junction, thus facilitating charge migration and utilization throughout the interconnected architectures. Second, there is a more compact space occupation of materials through a larger interstitial space, which ensures high electrode/electrolyte area to reduce the interface transfer resistance. When in contact with the electrolyte, band bending forms at the junction and extends to the rest of the coating, giving rise to the depletion region where charges yielded by incident photons are separated. Photogenerated electrons are readily transported away, and the photogenerated holes are transferred to the electrolyte for chemical reactions. Considering the fact that the surface reaction is directly related to the surface area and the macro-mesoporous structure possesses open-edge geometry plus a high surface-to-volume ratio, the locations of active sites can be maximized; in other words, the surface reaction is accelerated. Moreover, the open-edge geometry is beneficial for improving the efficiency in elimination of produced O_2 from the pores. A part of the O_2 generated in the disordered pores cannot eliminate from the pore and consequently decreases the photocurrent. This is more significant for photoelectrodes to retain photocurrent after long-time illumination. Third, partially substituting V^{5+} with Mo^{6+} can increase the charge carrier concentration for the host lattice intrinsically, leading to higher electrical conductivity than bare $BiVO_4$ photoelectrodes. Overall, we can understand the synergistic effects of composition regulation and morphology innovation more clearly from the enhancement factors of the solar-to-hydrogen conversion efficiencies (η_{STH}; see Figure S8 for details) and IPCE in Figure 6, which are defined as the ratio of the efficiencies of various $BiVO_4$-based films to that of the $BiVO_4$-disordered porous film. At the bias of 0.6 V *vs* Ag/AgCl, the η_{STH} enhancement factor (Figure 6a) for Mo:$BiVO_4$ macro-mesoporous film is 6.9, while the factors for $BiVO_4$ macro-mesoporous film and Mo:$BiVO_4$-disordered porous film are 3.4 and 1.7. The synergistic effect is obviously larger than simple composition regulation or simple morphology innovation. Moreover, the η_{STH} enhancement factor between Mo:$BiVO_4$

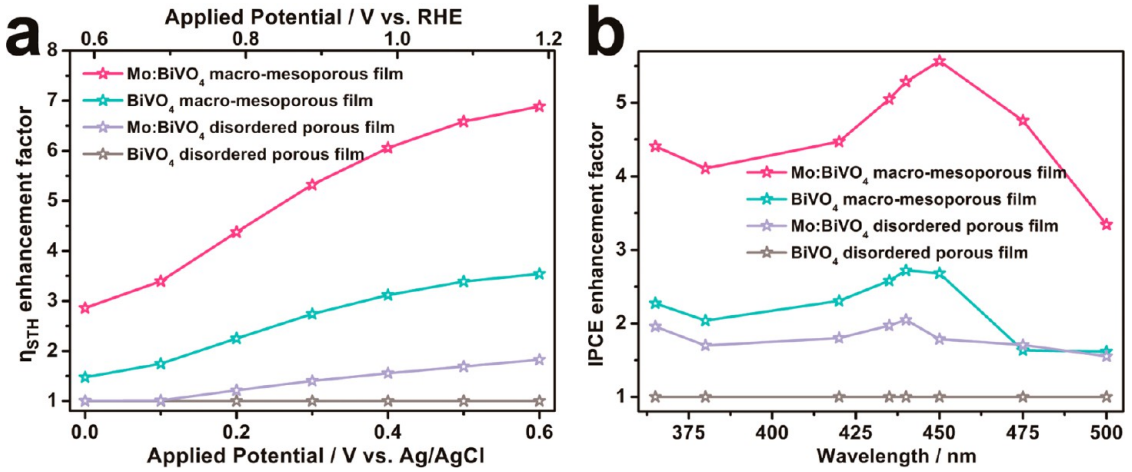

Figure 6. Enhancement factors of (a) solar-to-hydrogen conversion efficiencies (η_{STH}) and (b) IPCEs at 1.0 V *vs* Ag/AgCl, which are defined as the ratio of the efficiencies of various $BiVO_4$-based films to that of the $BiVO_4$-disordered porous film.

macro-mesoporous film and Mo:$BiVO_4$-disordered porous film is 4.1, which is larger than the factor between $BiVO_4$ macro-mesoporous $BiVO_4$-disordered porous film (3.4). The IPCE enhancement factors and η_{STH} enhancement factors at other biases all mirror the substantial enhancement, indicating that the influences of morphology innovation are more advantageous for the photoelectrodes with faster charge transport.

CONCLUSION

In conclusion, three-dimensional ordered macro-mesoporous Mo:$BiVO_4$ architectures are fabricated for PEC water splitting. With the help of a modified solution infiltration method and adjustable post-heating time, we can realize the incorporation of additional mesoscale pores into a periodic macroporous host scaffold. Three-dimensional ordered macro-mesoporous architecture possesses a more compact space occupation of materials through a larger interstitial space, which minimizes the inner resistance of charge transport and the contact resistance at the electrode/electrolyte and electrode/current collector junction. The efficiency in elimination of produced O_2 is also increased. Then the approach of precursor infiltration facilitates the composition regulation, so we can further substitute V^{5+} with Mo^{6+} to further optimize the charge migration of $BiVO_4$. The superior PEC performances and the analysis of EIS further prove that the charge migration is optimized. All of the results highlight the synergistic effect of nanoengineering from composition regulation and morphology innovation. This approach is helpful for creating more purpose-designed photoelectrodes with highly efficient performance.

EXPERIMENTAL SECTION

Fabrication of PS Colloidal Crystal Templates. FTO glass was cleaned under sonication by sequentially immersing in ethanol, acetone, and distilled water, and then treated with the $H_2SO_4/H_2O_2/H_2O$ (3:1:1, volume ratio) solution for a few seconds to make them uniformly hydrophilic. The well-ordered colloidal crystal templates comprising polystyrene spheres (PSs) arranged on a face-centered cubic lattice were fabricated using the methods of vertical deposition. The substrates were immersed vertically in the 0.5 wt % polystyrene latex at 60 °C. The drying of the sample at very low speed in the presence of moisture prevented the occurrence of cracking on the sample. Then the templates consisting of 200 nm PSs were heated at 110 °C for 0, 3, and 10 min.

Fabrication of Mo:$BiVO_4$ Films. In a typical procedure, $Bi(NO_3)_3 \cdot 5H_2O$ (0.5 mmol), $(NH_4)_6Mo_7O_{24} \cdot 4H_2O$ (0.0014 mmol), and NH_4VO_3 (0.49 mmol) were dissolved in 5 mL of nitric acid and 5 mL of distilled water. Then the mixed solution was diluted with 10 mL of ethanol. During the infiltration process, the lower edge of whole sandwich-like integration was immersed into the precursor solution vertically; hence, the solution could be penetrated into the interstices of the template *via* capillary force. After being dried at room temperature in vacuum, the samples were annealed at 500 °C for 2 h with a ramping rate of 2 °C min^{-1} to remove the PS template. For comparison, with respect to $BiVO_4$ three-dimensional structure, all of the steps were similar to Mo:$BiVO_4$ except precursor solution. In a typical procedure, $Bi(NO_3)_3 \cdot 5H_2O$ (0.5 mmol) and NH_4VO_3 (0.5 mmol) were dissolved in 5 mL of nitric acid and 5 mL of distilled water. Then the mixed solution was diluted with 10 mL of ethanol. The disordered porous film was prepared by drop-coating and calcination at 500 °C for 2 h with the ramping rate of 2 °C min^{-1}. $Bi(NO_3)_3 \cdot 5H_2O/NH_4VO_3$ and $Bi(NO_3)_3 \cdot 5H_2O/NH_4VO_3/(NH_4)_6Mo_7O_{24} \cdot 4H_2O$ were dissolved in distilled water as the precursor solution using the same atomic ratio.

Characterization. The X-ray diffraction (XRD) patterns were recorded by using a Philips XQPert Pro Super diffractometer with Cu Kα radiation (λ = 0.154178 nm). The field emission scanning electron microscopy images were performed by a JEOL JSM-6700F field emission scanning electron microscope (15 kV). The solid-state current−voltage (*I*−*V*) measurements in the dark were measured on an electrochemical station (CHI660B, Shanghai Chenhua Limited, China). Silver paste was used to make connections from the current−voltage testing system to the bottom FTO substrate, and the top Mo:$BiVO_4$ layer is in a double-probe configuration and set as voltage bias mode. The distance between the electrodes and between electrode and the edge of the film were both kept the same.

Photoelectrochemical Measurement. Photoelectrochemical test systems were composed of a standard three-electrode configuration. The Mo:$BiVO_4$ films with a Pt counter electrode and a Ag/AgCl reference electrode were immersed in a degassed 0.5 mol L^{-1} Na_2SO_4 buffer at pH 6.6, which had been purged with nitrogen for 15 min prior to the measurement. The photoelectrochemical characterizations, electrochemical impedance measurements, and open-circuit voltage decay were measured on an electrochemical station (CHI660B, Shanghai Chenhua Limited, China) under illumination using a 300 W Xe lamp under illumination from the back (glass) side of the film. The monochromatic light was filtered by filter plates for different wavelengths with a bandwidth of 10 nm and transmittance of 80%, and the monochromatic light power density was measured by a UV−vis irradiatometer with an accuracy of 1 μW cm^{-2}. The potential was swept at a sweep rate of 10 mV s^{-1}. The measured potentials *vs* Ag/AgCl were converted to the reversible hydrogen electrode (RHE) scale according to the Nernst equation: $E_{RHE} = E_{Ag/AgCl} + 0.0591pH + 0.1976$. Absorbed photon-to-electron conversion efficiency can be expressed as APCE = IPCE/$(1 - 10^{-A})$, where A is the absorption of the film at a specific wavelength. The solar-to-hydrogen conversion efficiencies (η_{STH}) are estimated from the Gibbs free energy, $\eta_{STH} = J \times (E_{rev}^{\circ} - V_{bias})/I$, which accounts for the thermodynamic losses associated with application of an external anodic bias and assumes 100% faradaic effciency. V_{bias} is the external anodic bias; J is photocurrent density (mA cm^{-2}) at V_{bias}; E_{rev}° is the standard reversible potential which is 1.23 V *vs* RHE; and I is the light intensity of light source (mW cm^{-2}).

Conflict of Interest: The authors declare no competing financial interest.

Acknowledgment. This work was financially supported by the National Natural Science Foundation of China (21331005, 11321503), and Chinese Academy of Science (XDB01010300), European Research Council (ThreeDsurface: 240144), BMBF (ZIK-3DNanoDevice: 03Z1MN11), BMBF (Meta-ZIK-BioLithoMorphie: 03Z1M511), and Volkswagen-Stiftung (Herstellung funktionaler Oberflächen: I/83 984).

Supporting Information Available: Figure S1−S5 represent typical characterization of macro-macroporous Mo:$BiVO_4$ architecture, disordered porous Mo:$BiVO_4$ architecture, macro-mesoporous $BiVO_4$ architecture, and disordered porous $BiVO_4$ architecture. Figure S6 is XRD data from representative $BiVO_4$ and Mo:$BiVO_4$ films. Figure S7 is Mott−Schottky plots of Mo:$BiVO_4$ macro-macroporous film and disordered porous film. Figure S8 is the solar-to-hydrogen conversion efficiencies of various $BiVO_4$-based films. This material is available free of charge *via* the Internet at http://pubs.acs.org.

REFERENCES AND NOTES

1. Fujishima, A.; Honda, K. Electrochemical Photolysis of Water at a Semiconductor Electrode. *Nature* **1972**, *238*, 37–38.
2. Turner, J. A. A Realizable Renewable Energy Future. *Science* **1999**, *285*, 687–689.
3. Grätzel, M. Photoelectrochemical Cells. *Nature* **2001**, *414*, 338–344.
4. Khan, S. U. M.; Al-Shahry, M.; Ingler, W. B. Efficient Photochemical Water Splitting by a Chemically Modified n-TiO_2. *Science* **2002**, *297*, 2243–2245.
5. Chen, X.; Ye, J.; Ouyang, S.; Kako, T.; Li, Z.; Zou, Z. Enhanced Incident Photon-to-Electron Conversion Efficiency of Tungsten Trioxide Photoanodes Based on 3D-Photonic Crystal Design. *ACS Nano* **2011**, *5*, 4310–4318.
6. Walter, M. G.; Warren, E. L.; McKone, J. R.; Boettcher, S. W.; Mi, Q.; Santori, E. A.; Lewis, N. S. Solar Water Splitting Cells. *Chem. Rev.* **2010**, *110*, 6446–6473.
7. Zhou, M.; Lou, X. W.; Xie, Y. Two-Dimensional Nanosheets for Photoelectrochemical Water Splitting: Possibilities and Opportunities. *Nano Today* **2013**, *8*, 598–618.
8. Liu, R.; Lin, Y.; Chou, L. Y.; Sheehan, S. W.; He, W.; Zhang, F.; Hou, H. J. M.; Wang, D. Water Splitting by Tungsten Oxide Prepared by Atomic Layer Deposition and Decorated with an Oxygen-Evolving Catalyst. *Angew. Chem., Int. Ed.* **2011**, *50*, 499–502.
9. Zhou, M.; Zhang, S.; Sun, Y.; Wu, C.; Wang, M.; Xie, Y. C-Oriented and {010} Facets Exposed $BiVO_4$ Nanowall Films: Template-Free Fabrication and Their Enhanced Photoelectrochemical Properties. *Chem.—Asian J.* **2010**, *5*, 2515–2523.
10. Kudo, A.; Omori, K.; Kato, H. A Novel Aqueous Process for Preparation of Crystal Form-Controlled and Highly Crystalline $BiVO_4$ Powder from Layered Vanadates at Room Temperature and Its Photocatalytic and Photophysical Properties. *J. Am. Chem. Soc.* **1999**, *121*, 11459–11467.
11. Zhao, Z.; Li, Z.; Zou, Z. Electronic Structure and Optical Properties of Monoclinic Clinobisvanite $BiVO_4$. *Phys. Chem. Chem. Phys.* **2011**, *13*, 4746–4753.
12. Walsh, A.; Yan, Y.; Huda, M. N.; Al-Jassim, M. M.; Wei, S. H. Band Edge Electronic Structure of $BiVO_4$: Elucidating the Role of the Bi s and V d Orbitals. *Chem. Mater.* **2009**, *21*, 547–551.
13. Xie, Y.; Sun, Y.; Qu, B.; Liu, Q.; Gao, S.; Yan, Z.; Yan, W.; Pan, B. C.; Wei, S. Highly Efficient Visible-Light-Driven Photocatalytic Activities in Synthetic Ordered Monoclinic $BiVO_4$ Quantum Tubes-Graphene Nanocomposites. *Nanoscale* **2012**, *4*, 3761–3767.
14. Zhou, M.; Bao, J.; Bi, W.; Zeng, Y.; Zhu, R.; Tao, M.; Xie, Y. Efficient Water Splitting *via* a Heteroepitaxial $BiVO_4$ Photoelectrode Decorated with Co-Pi Catalysts. *ChemSusChem* **2012**, *5*, 1420–1425.
15. Yang, S.; Lei, Y. Recent Progress on Surface Pattern Fabrications Based on Monolayer Colloidal Crystal Templates and Related Applications. *Nanoscale* **2011**, *3*, 2768–2782.
16. Jo, W. J.; Jang, J. W.; Kong, K. J.; Kang, H. J.; Kim, J. Y.; Jun, H.; Parmar, K. P. S.; Lee, J. S. Phosphate Doping into Monoclinic $BiVO_4$ for Enhanced Photoelectrochemical Water Oxidation Activity. *Angew. Chem., Int. Ed.* **2012**, *51*, 3147–3151.
17. Ye, H.; Park, H. S.; Bard, A. J. Screening of Electrocatalysts for Photoelectrochemical Water Oxidation on W-Doped $BiVO_4$ Photocatalysts by Scanning Electrochemical Microscopy. *J. Phys. Chem. C* **2011**, *115*, 12464–12470.
18. Berglund, S. P.; Rettie, A. J. E.; Hoang, S.; Mullins, C. B. Incorporation of Mo and W into Nanostructured $BiVO_4$ Films for Efficient Photoelectrochemical Water Oxidation. *Phys. Chem. Chem. Phys.* **2012**, *14*, 7065–7075.
19. Yang, S.; Xu, F.; Ostendorp, S.; Wilde, G.; Zhao, H.; Lei, Y. Template-Confined Dewetting Process to Surface Nanopatterns: Fabrication, Structural Tunability, and Structure-Related Properties. *Adv. Funct. Mater.* **2011**, *21*, 2446–2455.
20. Yang, S.; Lapsley, M. I.; Cao, B.; Zhao, C.; Zhao, Y.; Hao, Q.; Kiraly, B.; Scott, J.; Li, W.; Wang, L.; *et al.* Large-Scale Fabrication of Three-Dimensional Surface Patterns Using Template-Defined Electrochemical Deposition. *Adv. Funct. Mater.* **2013**, *23*, 720–730.
21. Pilli, S. K.; Furtak, T. E.; Brown, L. D.; Deutsch, T. G.; Turner, J. A.; Herring, A. M. Cobalt-Phosphate (Co-Pi) Catalyst Modified Mo-Doped $BiVO_4$ Photoelectrodes for Solar Water Oxidation. *Energy Environ. Sci.* **2011**, *4*, 5028–5034.
22. Liang, Y.; Tsubota, T.; Mooij, L. P. A.; van de Krol, R. Highly Improved Quantum Efficiencies for Thin Film $BiVO_4$ Photoanodes. *J. Phys. Chem. C* **2011**, *115*, 17594–17598.
23. Seabold, J. A.; Choi, K. S. Efficient and Stable Photooxidation of Water by a Bismuth Vanadate Photoanode Coupled with an Iron Oxyhydroxide Oxygen Evolution Catalyst. *J. Am. Chem. Soc.* **2012**, *134*, 2186–2192.
24. Zhong, D. K.; Choi, S.; Gamelin, D. R. Near-Complete Suppression of Surface Recombination in Solar Photoelectrolysis by "Co-Pi" Catalyst-Modified W:$BiVO_4$. *J. Am. Chem. Soc.* **2011**, *133*, 18370–18377.
25. van de Lagemaat, J.; Frank, A. J. Nonthermalized Electron Transport in Dye-Sensitized Nanocrystalline TiO_2 Films: Transient Photocurrent and Random-Walk Modeling Studies. *J. Phys. Chem. B* **2001**, *105*, 11194–11205.
26. Zhou, M.; Wu, H. B.; Bao, J.; Liang, L.; Lou, X. W.; Xie, Y. Ordered Macroporous $BiVO_4$ Architectures with Controllable

Dual Porosity for Efficient Solar Water Splitting. *Angew. Chem., Int. Ed.* **2013**, *52*, 8579–8583.
27. Sakamoto, J. S.; Dunn, B. Hierarchical Battery Electrodes Based on Inverted Opal Structures. *J. Mater. Chem.* **2002**, *12*, 2859–2861.
28. Rouquerol, J.; Avnir, D.; Fairbridge, C. W.; Everett, D. H.; Haynes, J. M.; Pernicone, N.; Ramsay, J. D. F.; Sing, K. S. W.; Unger, K. K. Recommendations for the Characterization of Porous Solids (Technical Report). *Pure Appl. Chem.* **1994**, *66*, 1739–1758.
29. Du, J.; Lai, X.; Yang, N.; Zhai, J.; Kisailus, D.; Su, F.; Wang, D.; Jiang, L. Hierarchically Ordered Macro-mesoporous TiO_2—Graphene Composite Films: Improved Mass Transfer, Reduced Charge Recombination, and Their Enhanced Photocatalytic Activities. *ACS Nano* **2010**, *5*, 590–596.
30. Liu, L.; Karuturi, S. K.; Su, L. T.; Tok, A. I. Y. TiO_2 Inverse-Opal Electrode Fabricated by Atomic Layer Deposition for Dye-Sensitized Solar Cell Applications. *Energy Environ. Sci.* **2011**, *4*, 209–215.
31. Zhou, M.; Bao, J.; Tao, M.; Zhu, R.; Lin, Y.; Zhang, X.; Xie, Y. Periodic Porous Thermochromic VO_2(M) Films with Enhanced Visible Transmittance. *Chem. Commun.* **2013**, *49*, 6021–6023.
32. Li, Y.; Cai, W.; Cao, B.; Duan, G.; Li, C.; Sun, F.; Zeng, H. Morphology-Controlled 2D Ordered Arrays by Heating-Induced Deformation of 2D Colloidal Monolayer. *J. Mater. Chem.* **2006**, *16*, 609–612.
33. Sivula, K.; Le Formal, F.; Grätzel, M. Solar Water Splitting: Progress Using Hematite (α-Fe_2O_3) Photoelectrodes. *ChemSusChem* **2011**, *4*, 432–449.
34. Momma, K.; Izumi, F. VESTA 3 for Three-Dimensional Visualization of Crystal, Volumetric and Morphology Data. *J. Appl. Crystal.* **2011**, *44*, 1272–1276.
35. a) Hong, S. J.; Lee, S.; Jang, J. S.; Lee, J. S. Heterojunction $BiVO_4$/WO_3 Electrodes for Enhanced Photoactivity of Water Oxidation. *Energy Environ. Sci.* **2011**, *4*, 1781–1787. b) Yang, S. C.; Yang, D. J.; Kim, J.; Hong, J. M.; Kim, H. G.; Kim, I. D.; Lee, H. Hollow TiO_2 Hemispheres Obtained by Colloidal Templating for Application in Dye-Sensitized Solar Cells. *Adv. Mater.* **2008**, *20*, 1059–1064.
36. Luo, W.; Yang, Z.; Li, Z.; Zhang, J.; Liu, J.; Zhao, Z.; Wang, Z.; Yan, S.; Yu, T.; Zou, Z. Solar Hydrogen Generation from Seawater with a Modified $BiVO_4$ Photoanode. *Energy Environ. Sci.* **2011**, *4*, 4046–4051.
37. a) Long, M.; Cai, W.; Kisch, H. Visible Light Induced Photoelectrochemical Properties of n-$BiVO_4$ and n-$BiVO_4$/p-Co_3O_4. *J. Phys. Chem. C* **2007**, *112*, 548–554. b) Zhang, L. W.; Wang, Y. J.; Cheng, H. Y.; Yao, W. Q.; Zhu, Y. F. Synthesis of Porous Bi_2WO_6 Thin Films as Efficient Visible-Light-Active Photocatalysts. *Adv. Mater.* **2009**, *21*, 1286–1290.
38. Cheng, C.; Karuturi, S. K.; Liu, L.; Liu, J.; Li, H.; Su, L. T.; Tok, A. I. Y.; Fan, H. J. Quantum-Dot-Sensitized TiO_2 Inverse Opals for Photoelectrochemical Hydrogen Generation. *Small* **2012**, *8*, 37–42.
39. Ng, Y. H.; Iwase, A.; Kudo, A.; Amal, R. Reducing Graphene Oxide on a Visible-Light $BiVO_4$ Photocatalyst for an Enhanced Photoelectrochemical Water Splitting. *J. Phys. Chem. Lett.* **2010**, *1*, 2607–2612.
40. Zhou, M.; Bao, J.; Tao, M.; Zhu, R.; Zeng, Y.; Wei, Z.; Xie, Y. Rational Design of the Nanowall Photoelectrode for Efficient Solar Water Splitting. *Chem. Commun.* **2012**, *48*, 3439–3441.